

Method for overcoming the finite space-bandwidth limitation of digital holograms in holography

BYUNG GYU CHAE

Holographic Contents Research Laboratory, Electronics and Telecommunications Research Institute, 218 Gajeong-ro, Yuseong-gu, Daejeon 34129, Republic of Korea
bgchae@etri.re.kr

Abstract:

A digital hologram has a finite space-bandwidth, which determines the spatial resolution and angular field of view of its reconstructed image. However, higher space-bandwidth induces aliased replica patterns in the Fresnel diffraction. This study analyzes the spatial distribution of the angular spectrum in an undersampled hologram using angle modulation in the complex domain. The replica functions are identified as phase-modulated functions by multiples of the sampling frequency, with the spatial frequency range extending continuously from the original function into the regions of the replica functions. Simulations of optical imaging confirm the theoretical predictions, demonstrating that imaging performance beyond the space-bandwidth limitation of a digital hologram is achievable. Specifically, high-order diffraction fields have the orthogonal property, which enables the effective removal of them. This approach provides an alternative solution to overcome the constraints imposed by the finite space-bandwidth of digital holograms.

© 2025 Optica Publishing Group

1. Introduction

The holographic image is reconstructed either numerically or optically from the digital hologram. A digital hologram has a finite space-bandwidth, which determines key imaging performance metrics such as the resolution limit and angular field of view [1, 2]. The space-bandwidth B_w of the Fresnel hologram sampled at Δ pixel interval with $N \times N$ pixels is represented as

$$B_w = \frac{N\Delta}{\lambda z}. \quad (1)$$

According to the Abbe diffraction theory, the resolution limit R_{lim} of the reconstructed image is given as the reciprocal of this value, $R_{\text{lim}} = \frac{\lambda z}{N\Delta} = \frac{\lambda}{2 \sin \theta}$ [3–6]. In optical reconstruction, the viewing angle is twice the angle value θ . The hologram aperture constrains the ability to capture the spatial frequency components of the diffractive wave.

Aliased replica patterns are formed when the required bandwidth exceeds the bandwidth supported by the hologram's pixel [7–10]. Spatial frequency components higher than the Nyquist frequency are aliased, making them appear as lower frequency components of the original function. The spatial frequency f increases linearly along the spatial direction, and the aliased frequency f_a is determined by the relationship [11]:

$$f_a = |f - n f_s|, \quad (2)$$

where f_s is the sampling frequency and n is an integer. This property results in the formation of replica functions that are spatially distributed at regular periodic intervals. Figure 1 illustrates the aliasing phenomenon for a point-source hologram sampled at a lower sampling rate. The complex-valued hologram $g(x, y)$ for a point object $\delta(x, y)$ is expressed as the impulse response

function, $g(x, y) = \frac{e^{ikz}}{i\lambda z} \exp \left[\frac{i\pi}{\lambda z} (x^2 + y^2) \right]$. Using the modulated form of the Fourier-transformed function, the sampled hologram at an interval Δx along the x -axis is written as follows [12, 13]:

$$\sum_n g(n\Delta x) \delta(x - n\Delta x) = \frac{1}{\Delta x} \sum_n c_n g \left(x + \frac{\lambda z n}{\Delta x} \right). \quad (3)$$

For simplicity, a one-dimensional description is used hereafter. The angular spectra, within the range of the original function, are folded at intervals determined by the folding frequency. Continuous response functions are obtained through the inverse Fourier transform of modulated angular spectra. The replication pattern are formed at a reduced period of $\frac{\lambda z}{s\Delta x}$ when undersampled by a factor s of Δx .

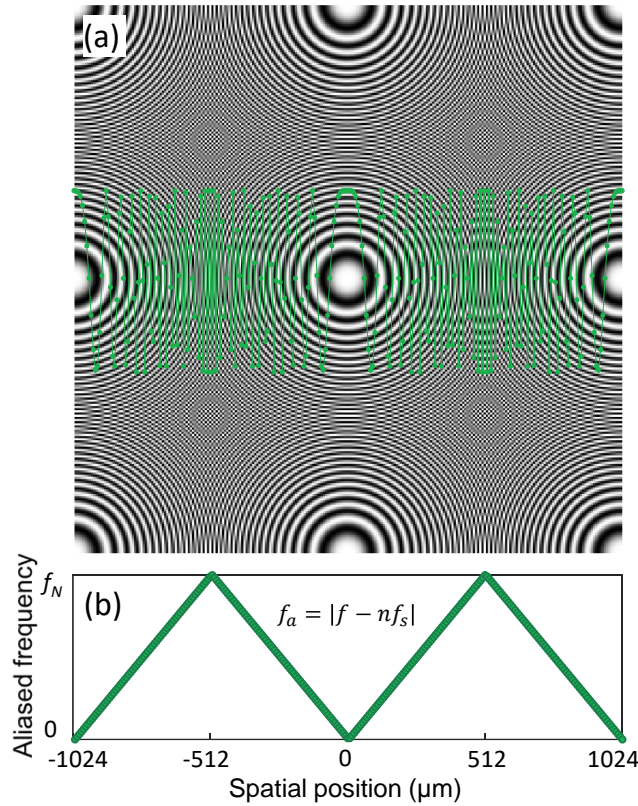


Fig. 1. Aliasing phenomenon for a point-source hologram sampled at a lower sampling rate. (a) The real-valued hologram made at a distance of a half of z_c exhibits four replica Fresnel zones. The inset graph is the 1D quadratic phase function along the lateral distance at the center. (b) Aliased frequencies for the quadratic phase function.

Previously, it was reported that this type of hologram reconstructs a holographic image with a space-bandwidth that spans the entire aperture of the digital hologram, regardless of aliased fringes [6, 13–15]. This suggests that the replica functions correspond to the high spatial-frequency components of the hologram field. However, the above description of aliasing makes it difficult to explain numerical and experimental results. The space-bandwidth remains confined to the original function due to replication, meaning that the diffraction performance is limited to its initial value. As a result, establishing a unified understanding in this field has proven challenging to date.

In this study, an angular spectrum in the undersampled hologram with aliased replica fringes is investigated using angle modulation in the complex plane. The replica functions exhibit a phase modulation pattern created by a carrier wave that corresponds to multiples of the sampling frequency. The spatial frequency increases linearly across the region of the replica functions. The replica function plays a role in the higher frequency components of original function, as well as additive replication. Numerical simulation of optical imaging reveals a consistency of this scheme, and furthermore, an approach to suppress high-order diffractions from their orthogonal properties is studied.

2. Angular spectrum distribution in the undersampled hologram

2.1. Spatial frequency in complex plane

The spatial frequency in the Fresnel hologram is represented as $\frac{x}{\lambda z}$ from the quadratic phase term, which depends linearly on the lateral spatial distance. The distribution of spatial frequency in the undersampled hologram of a point source is investigated, particularly in the complex plane. The complex-valued hologram, consisting of 256×256 pixels with a $8\text{-}\mu\text{m}$ pixel pitch, was synthesized using the Fresnel diffraction formula with a single Fourier transform. A unit-amplitude plane wave with a wavelength λ of 532 nm was used. The hologram of a point object placed at a distance of a half of z_c results in the formation of four replica Fresnel zones, as shown in Fig 1(a). The critical distance z_c is the minimum distance at which hologram functions are free from replication effects:

$$z_c = \frac{N\Delta x^2}{\lambda}, \quad (4)$$

where the replication interval $\frac{\lambda z}{\Delta x}$ in Eq. (3) equals the field extent $N\Delta x$. No aliased fringes appear for distances above z_c . For this configuration, z_c is calculated to be 30.8 mm .

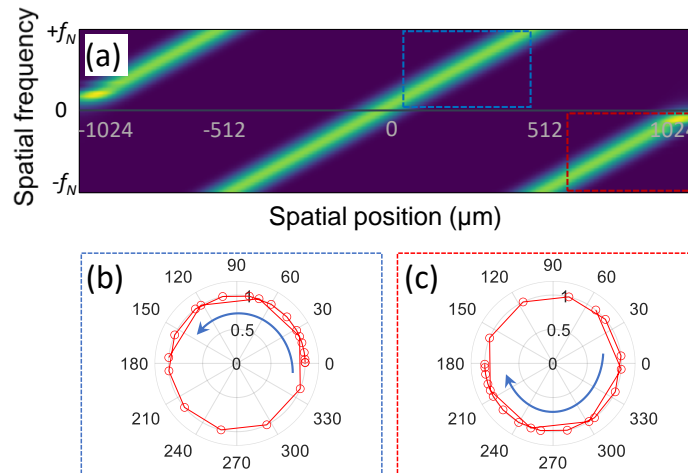


Fig. 2. Spatial frequency distribution of an undersampled point-source hologram in the complex domain. (a) Spatial frequency variation along the lateral spatial position. The trajectories of the position vectors (b) in the blue box and (c) in the red box, corresponding to those in Fig. 2(a), are plotted in polar coordinates, respectively.

Figure 2 illustrates the change in spatial frequency along the lateral distance. The spatial frequency along the x -axis at the center of the hologram is obtained using a commercial spectrum calculation program, in Fig. 2(a). Unlike the aliased frequencies in the real domain, both negative

and positive spatial frequency components appear in the complex plane. In the complex-valued function, the position vector with negative frequencies rotates clockwise, while the position vector with positive frequencies rotates counterclockwise.

The spatial frequency exhibits a linear dependence on the lateral spatial distance. On the positive-axis side, the spatial frequency increases continuously up to the Nyquist frequency, i.e., $f_N = 1.25 \times 10^5 \text{m}^{-1}$. The position of the Nyquist frequency is estimated to be $x = 512 \mu\text{m}$ using Eq. (1). At this point, the spatial frequency changes discontinuously to the negative Nyquist value, then continues to increase toward zero. The trajectories of the position vectors in these two distinct regions are plotted in polar coordinate, as depicted in Figs. 2(b) and 2(c). The position vector rotates from a counterclockwise direction to a clockwise direction at the Nyquist frequency. Similarly, the negative side shows symmetrical behavior.

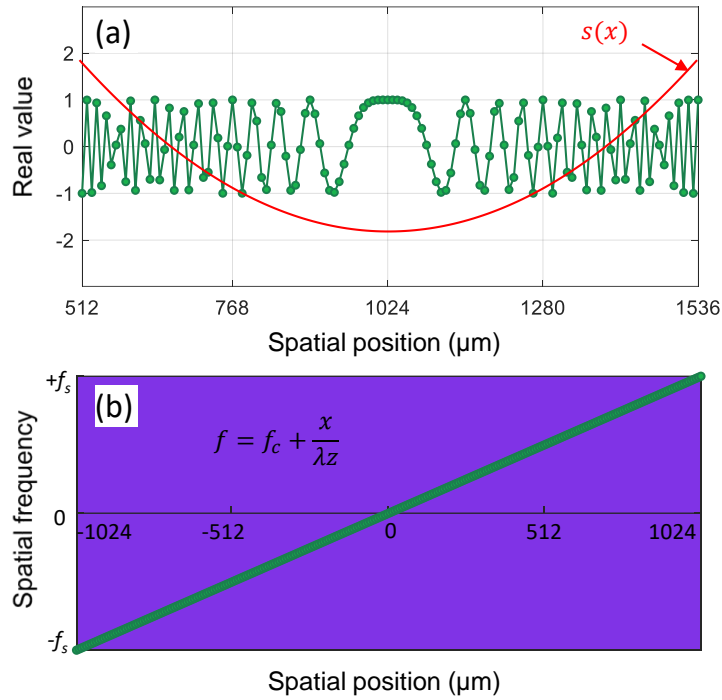


Fig. 3. Spatial frequency distribution after considering modulation form by a carrier wave. (a) The phase profile of the carrier wave modulated by the modulating signal at the +1st-order shifted position. The modulating signal is inserted at an arbitrary position. (b) The spatial frequency as a function of spatial position.

2.2. Angle modulation in the undersampled hologram

The spatial frequency distribution in an undersampled hologram can be interpreted using angle modulation in the complex plane. The shifted replica function in Eq. (3) is described as a phase-modulated function by a carrier wave:

$$c_{ng} \left(x + \frac{\lambda z n}{\Delta x} \right) = \exp \left[i 2\pi \left(\frac{nx}{2\Delta x} + \frac{x^2}{2\lambda z} \right) \right]. \quad (5)$$

In the phase modulation [11], the instantaneous phase $\phi(x)$ is given by

$$\phi(x) = 2\pi f_c x + D_o s(x), \quad (6)$$

where the carrier wave is a sinusoidal wave with a carrier frequency, $f_c = n \left(\frac{1}{2\Delta x} \right)$, expressed as $e^{-\frac{in\pi x}{\Delta x}}$, and the modulation index D_o is equal to one.

The modulating signal $s(x)$ in the above equation is a simple quadratic function:

$$s(x) = \frac{\pi x^2}{\lambda z}. \quad (7)$$

The phase of the carrier wave is modulated by the modulating signal, leading to the formation of a replica zone, which appears as moiré fringes shifted to $\frac{\lambda z n}{\Delta x}$. Figure 3(a) shows the +1st-order replica function shifted to a position of 1024 μm . Since the amplitude of the phase-modulated wave remains constant, the average power of the spatially distributed wave is one half.

The instantaneous frequency in phase modulation is calculated from the derivative of phase value:

$$f = \frac{1}{2\pi} \frac{d\phi(x)}{dx} = f_c + D_o \frac{ds(x)}{dx} = f_c + \frac{x}{\lambda z}. \quad (8)$$

The spatial frequency f is the sum of the original frequency $\frac{x}{\lambda z}$ and the carrier frequency. Here, the carrier frequency is a multiple of the sampling frequency. Figure 3(b) draws the angular spectrum distribution considering the modulation behaviour. The spatial frequency on both sides of the x -axis increases from zero to the sampling frequency of $f_s = 2.5 \times 10^5 \text{ m}^{-1}$ without any discontinuity.

Likewise, all shifted replica functions can be expressed as higher spatial-frequency components corresponding to those of the original function. This analysis in the complex plane demonstrates that the shifted replica function represents not only aliased fringes but also higher spectral components. Although the description focuses on the central function, it applies equally to the adjacent functions. It is interesting because the spatial frequency is relative depending on the criteria. Consequently, the spatial-frequency components of each function should be still the high-frequency components of adjacent functions.

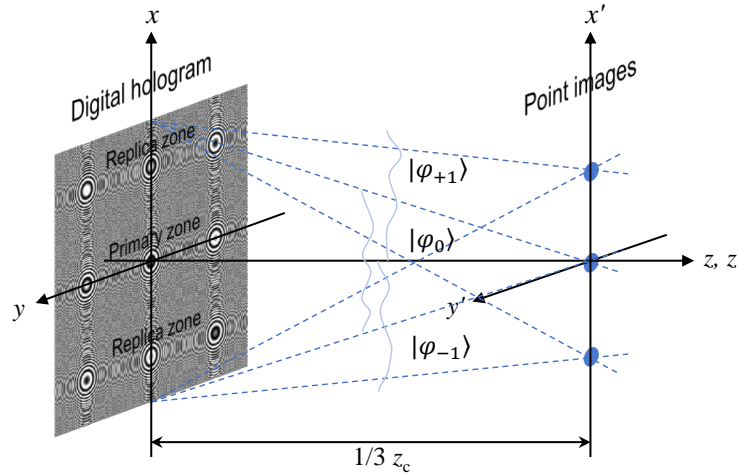


Fig. 4. Schematic diagram illustrating high-order diffractions from an undersampled hologram. Point-image reconstruction is described using a hologram made at one-third of z_c . For clarity, high-order diffractions for three Fresnel zones in the central region are drawn.

3. High-order diffraction fields in undersampled holograms

3.1. Orthogonality property of high-order diffraction fields

The plane wave incident on an undersampled hologram generates high-order images in the image plane, as illustrated in Fig. 4. For clarity, the high-order diffractions for three Fresnel zones, created at one-third of z_c , are depicted. Evidently, each image is reconstructed using the entire aperture of the digital hologram.

The diffraction function $|\psi\rangle$ for the undersampled hologram consists of spatial image states $|\varphi\rangle$ corresponding to individual Fresnelets:

$$\psi = \sum_q \alpha_q |\varphi_q\rangle, \quad (9)$$

where α_q represents the probability coefficient. These coefficients are equal from the fact that point images exhibit uniformly distributed intensity. It is important that the spatial image states are eigenfunctions, as any function can be expressed as a complete set formed by their linear combination. The eigenfunctions are orthogonal, verified by the inner product of spatial image states:

$$\langle \varphi_m | \varphi_n^* \rangle = \iint_{-\infty}^{\infty} \varphi_m(x', y') \varphi_n^*(x', y') dx' dy'. \quad (10)$$

The spatial image state can be calculated using the Fresnel diffraction formula. In a one-dimensional description, $\varphi_m(x')$ propagating to an arbitrary distance z_1 is given as

$$\varphi_n(x') = \frac{e^{-ikz_1}}{i\lambda z_1} \exp\left(-i\pi \frac{x'^2}{\lambda z_1}\right) \iint g_n(x) \exp\left(-i\pi \frac{x^2}{\lambda z_1}\right) \exp\left(2i\pi \frac{x'x}{\lambda z_1}\right) dx. \quad (11)$$

Substituting $g_n(x) = \exp\left[i\pi \left(\frac{x^2}{\lambda z} + \frac{nx}{\Delta x}\right)\right]$ from Eq. (5), above equation becomes

$$\varphi_n(x') = \frac{e^{-ikz_1}}{i\lambda z_1} \exp\left(-i\pi \frac{x'^2}{\lambda z_1}\right) \exp\left(-i\pi \frac{b^2}{a\lambda^2 z_1^2}\right) \iint \exp\left[i\pi a \left(x + \frac{b}{a\lambda z_1}\right)^2\right] dx, \quad (12)$$

where $a = \frac{1}{\lambda z} - \frac{1}{\lambda z_1}$ and $b = x' + \frac{\lambda z_1 n}{2\Delta x}$. The integral evaluates to $\sqrt{\frac{i}{a}}$ using contour integration:

$$\varphi_n(x') = \frac{e^{-ikz_1}}{i\lambda z_1} \sqrt{\frac{i}{a}} \exp\left(-i\pi \frac{x'^2}{\lambda z_1}\right) \exp\left[-i\pi \frac{1}{a\lambda^2 z_1^2} \left(x' + \frac{\lambda z_1 n}{2\Delta x}\right)^2\right]. \quad (13)$$

The inner product of two state functions, $\int_{-\infty}^{\infty} \varphi_m(x') \varphi_n^*(x') dx'$, simplifies to a delta function:

$$\frac{1}{\lambda^2 z_1^2 a} \exp\left[-i\pi \frac{m^2 - n^2}{4a\Delta x^2}\right] \int_{-\infty}^{\infty} \exp\left[2i\pi \frac{x'(m-n)}{a\lambda z_1 2\Delta x}\right] dx' = \frac{2\Delta x}{\lambda z_1} \delta(m-n). \quad (14)$$

Extending this to two-dimensional space yields

$$\iint_{-\infty}^{\infty} \varphi_m(x', y') \varphi_n^*(x', y') dx' dy' = c_o^2 \delta_{mn}, \quad (15)$$

where $c_o = \frac{2\Delta x}{\lambda z_1}$. This result confirms that spatial image modes are orthogonal and serve as eigenstates of the diffraction function. Additionally, the image intensity is inversely proportional to the square of the propagation distance.

The diffraction fields from individual Fresnelets do not interfere with each other during wave propagation. Each diffraction beam independently forms the corresponding image without disturbance from other beams.

This interpretation applies to high-order diffractions generated from the properly sampled hologram. This orthogonal property enables the effective removal of high-order terms, commonly treated as noise, using appropriate external operations [14].

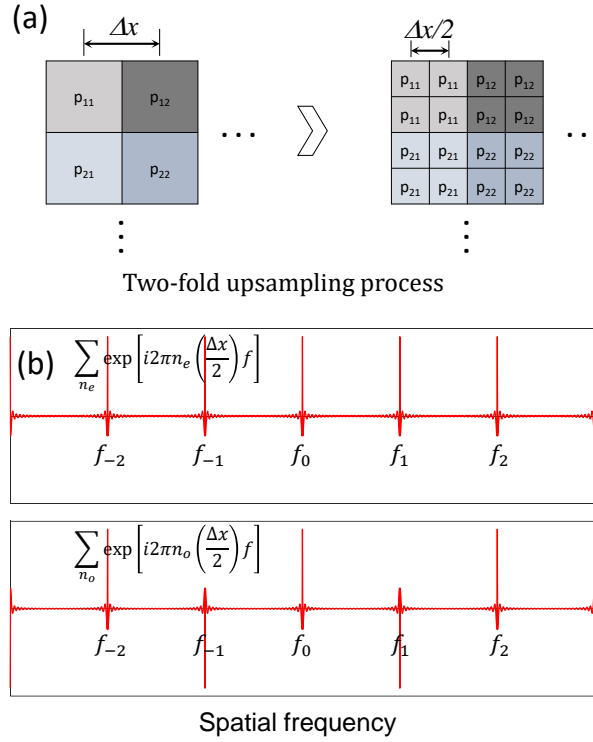


Fig. 5. Diffraction properties of an upsampled hologram. (a) The upsampling process of the sampled hologram. The two-fold upsampling is achieved by duplicating the pixel values of the original sampled hologram, where each pixel is subdivided into smaller sub-pixels, p_{mn} . (b) The Fourier spectra of Dirac comb functions corresponding to the sampling by even numbers n_e and odd numbers n_o are numerically calculated. The period of spatial frequencies is a multiple of $\frac{1}{\Delta x}$.

3.2. Suppression of high-order diffraction fields

The sampled hologram generates high-order diffractions due to its pixelated structure. The high-order terms in the Fresnel diffraction regime are characterized in terms of a periodic Fourier spectrum G [6]:

$$FT \left[\sum_n g(x) \delta(x - n\Delta x) \right] = G(f) \otimes FT \left[\sum_n \delta(x - n\Delta x) \right] = \frac{1}{\Delta x} \sum_q G \left(f - \frac{q}{\Delta x} \right), \quad (16)$$

where FT denotes the Fourier transform, and \otimes represents the convolution sign. The periodic Fourier spectrum is expressed using the Dirac comb distribution.

Figure 5 illustrates the diffraction properties of sampled hologram using a two-fold upsampling process. The upsampling process involves duplicating the pixel values of the original hologram, where each pixel in the original corresponds to four identical pixels in the upsampled version.

In this circumstance, the two-fold upsampled hologram can be divided into two components: one sampled by even numbers n_e and the other by odd numbers n_o , i.e., $\sum_{n_e} \delta \left(x - \frac{n_e \Delta x}{2} \right) + \sum_{n_o} \delta \left(x - \frac{n_o \Delta x}{2} \right)$. The corresponding pixels in both terms have the same value, but the odd term pixels are shifted by $\frac{\Delta x}{2}$.

Applying this description to the Fourier transform of the Dirac comb distribution in Eq. (16),

the function is written by

$$\mathbf{FT} \left[\sum_n \delta \left(x - \frac{n\Delta x}{2} \right) \right] = \sum_{n_e} \exp \left[i2\pi n_e \left(\frac{\Delta x}{2} \right) f \right] + \sum_{n_o} \exp \left[i2\pi n_o \left(\frac{\Delta x}{2} \right) f \right], \quad (17)$$

where a Dirac comb in frequency domain is expressed as a Fourier series. As shown in Fig. 5(b), Dirac delta functions in both terms have an opposite value at odd multiples of $\frac{1}{\Delta x}$, which is due to the shifted phase factor of $e^{2\pi i \left(\frac{\Delta x}{2} \right) f}$. Thus, both Fourier transform terms combine into a single function, $\sum_q \delta \left(f - \frac{2q}{\Delta x} \right)$, resulting in the removal of the $\pm 1^{\text{st}}$ -order peaks. The periodic Fourier spectrum of sampled hologram is then represented as

$$\mathbf{FT} [\dots] = \frac{2}{\Delta x} \sum_q G \left(f - \frac{2q}{\Delta x} \right). \quad (18)$$

The high-order spectra are generated at intervals of multiples of $\frac{2}{\Delta x}$. The Fourier space is expanded into two times. This type of upsampling process effectively suppresses corresponding high-order diffractive waves [6, 13].

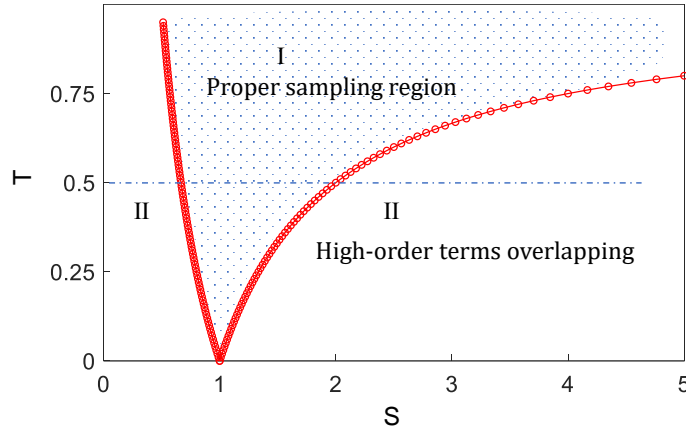


Fig. 6. Sampling conditions in numerical simulation of the Fresnel diffraction waves for the undersampled hologram. Numerical calculations conserving higher spatial-frequency components can be performed at all propagation distances.

4. Imaging behaviour of undersampled hologram

4.1. Sampling condition in numerical simulation

To observe the propagation behavior of the diffracted wave $\psi(x', y')$ from the undersampled hologram $g(x, y)$ to a far distance, it is essential to first investigate the sampling properties. The sampling condition in the Fresnel diffraction formula has been well established [10, 16–18]:

$$\psi(x', y') = \frac{ie^{-ikz_1}}{\lambda z_1} \exp \left[-i \frac{\pi}{\lambda z_1} (x'^2 + y'^2) \right] \mathbf{FT} \left[g(x, y) \exp \left[-i \frac{\pi}{\lambda z_1} (x^2 + y^2) \right] \right]. \quad (19)$$

Considering a point-source hologram, the quadratic phase term (QP) within the Fourier transform is expressed as

$$\text{QP} = \frac{e^{ikz}}{i\lambda z} \exp \left[i \frac{\pi}{\lambda} (x^2 + y^2) \left(\frac{1}{z} - \frac{1}{z_1} \right) \right]. \quad (20)$$

To avoid aliasing, the sampling rate f_s must exceed twice the maximum spatial frequency $f_{x,\max}$ of the phase term:

$$f_s \geq 2f_{x,\max} = \frac{2x_{\max}}{\lambda} \left(\frac{1}{z} - \frac{1}{z_1} \right). \quad (21)$$

Using a sampling rate of $\frac{1}{\Delta x}$ and the hologram's field size, $N\Delta x = 2|x_{\max}|$, the well-sampling condition with respect to the reconstruction distance z_1 is given by

$$\left| \frac{zz_1}{z_1 - z} \right| \geq z_c = \frac{N\Delta x^2}{\lambda}. \quad (22)$$

Substituting $z = Tz_c$ and $z_1 = Sz$, the left-hand tem of Eq. (22) can be rearranged as

$$\left| \frac{z}{1 - z/z_1} \right| = \left| \frac{Tz_c}{1 - 1/S} \right|. \quad (23)$$

Here, T and S are scaling factors. Incorporating Eq. (23) into Eq. (22), the sampling condition is represented as follows:

$$\frac{1}{1+T} \leq S \leq \frac{1}{1-T}. \quad (24)$$

As illustrated in Fig. 6, proper sampling is achievable within the intermediate region (I). High-order diffraction overlapping arises in the region (II), out of the proper sampling range.

Meanwhile, the replica functions preserve the higher spatial frequencies of the original function. Thus, while aliasing-induced high-order diffractions occur, numerical calculations that retain higher spatial-frequency components are feasible at all propagation distances.

4.2. Optical simulations

Figure 7 illustrates the imaging behavior for the undersampled hologram. The diffractive wave $\psi(x', y')$, propagating from the hologram function $g(x, y)$, was numerically calculated by using the Rayleigh-Sommerfeld diffraction formula [1]:

$$\psi(x', y') = \frac{i}{\lambda} \iint E_R(x, y) g(x, y) \frac{\exp(-ikr)}{r} dx dy, \quad (25)$$

where an incident plane wave with a unit amplitude, $E_R(x, y)$ is assumed, and k is the wavenumber of $2\pi/\lambda$. The intensity of the diffractive waves along the lateral line at the center is displayed as a function of the propagating distance, $r = \sqrt{z^2 + (x' - x)^2 + (y' - y)^2}$. The well-behaved waves propagate at all propagation distances without disturbance. Individual diffraction waves cannot be distinguished in the region close to the hologram. However, as previously stated, high-order diffractions do not interfere with each other because of their orthogonality, which results in the formation of the point images in the Fresnel diffraction region.

Figure 7(a) shows propagating waves from the point-source hologram synthesized at a half of z_c . In this case, the S ratio ranges from 0.67 to 2, based on Eq. (24). The proper sampling without overlapping of the $\pm 1^{\text{st}}$ -order diffractions appears in the region from 10.3 mm to 30.8 mm. These values well match with those in the numerical simulation. The point image is formed at a half of z_c , i.e., 15.4 mm, and then spreads out as it propagates further. The image resolution of $4 \mu\text{m}$ is twice as high as the hologram pixel size, and similarly, the spreading angle is double that of the diffraction angle of hologram pixel. The spreading angle is estimated to be approximately 7.6° , whereas the diffraction angle for a hologram pixel size of $8 \mu\text{m}$ is 3.8° .

The hologram made at a quarter of critical distance reconstructs the point image with a spatial resolution of $2 \mu\text{m}$, where the spreading angle, i.e., the viewing angle increases to 15.2° , in Fig. 7(b). The proper sampling area ranges from 6.2 mm to 10.3 mm, which agrees with the calculated quantities.

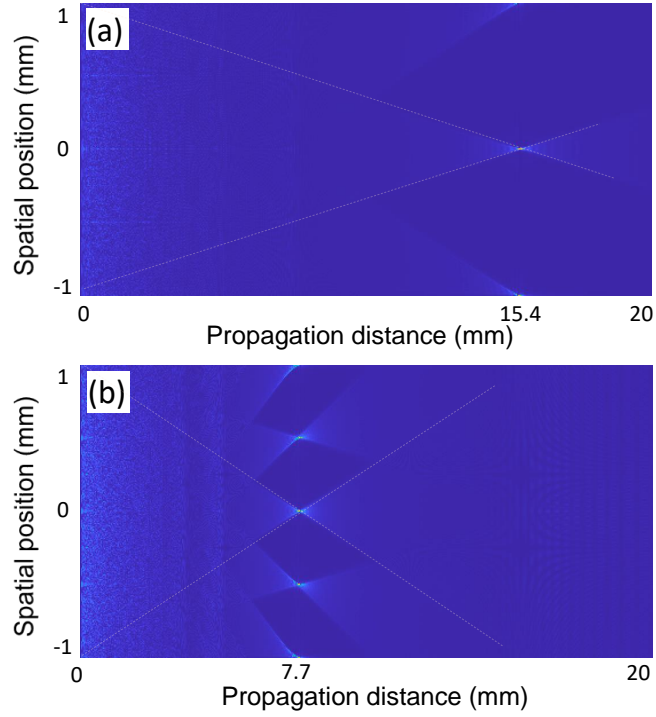


Fig. 7. Imaging behavior of an undersampled point-source hologram simulated using the Rayleigh-Sommerfeld diffraction formula. (a) Propagating waves from the hologram prepared using a point object placed at half- z_c . (b) Propagating waves from the hologram prepared using a point object placed at quarter- z_c . The intensity of the diffractive waves along the x -axis is displayed. The aspect ratio of the image is conveniently adjusted. Inset lines are included to clearly indicate the diffraction angle, 2θ .

Both the image resolution and spreading angle increase as the synthesis distance of the digital hologram decreases. It appears that the entire aperture of the digital hologram contributes to image formation, regardless of aliasing.

Meanwhile, the angular spectrum method allows the image space to be confined within the diffraction zone of a hologram pixel, effectively eliminating overlapping of high-order diffractions during numerical calculations. The algorithm involves a double Fourier transform [1, 6]:

$$\psi(x', y') = \mathbf{IFT} \left(\mathbf{FT} [E_R(x, y)g(x, y)] \exp [i\pi\lambda z(f_x^2 + f_y^2)] \right), \quad (26)$$

where \mathbf{IFT} indicates the inverse Fourier transform. The pixel resolutions in each space are governed by the sampling relation:

$$\Delta x' = \frac{1}{N\Delta f_x} = \Delta x. \quad (27)$$

The pixel values in both hologram and image planes are the same via the pixel value Δf_x in the intermediate Fourier plane. Only the zeroth-order region in the intermediate plane, $N\Delta f_x$ is utilized, thereby excluding high-frequency components beyond the diffraction limit.

Figure 8(a) presents the simulated diffractive waves obtained using the angular spectrum method. The high-frequency components of diffractions are removed due to an upper bound

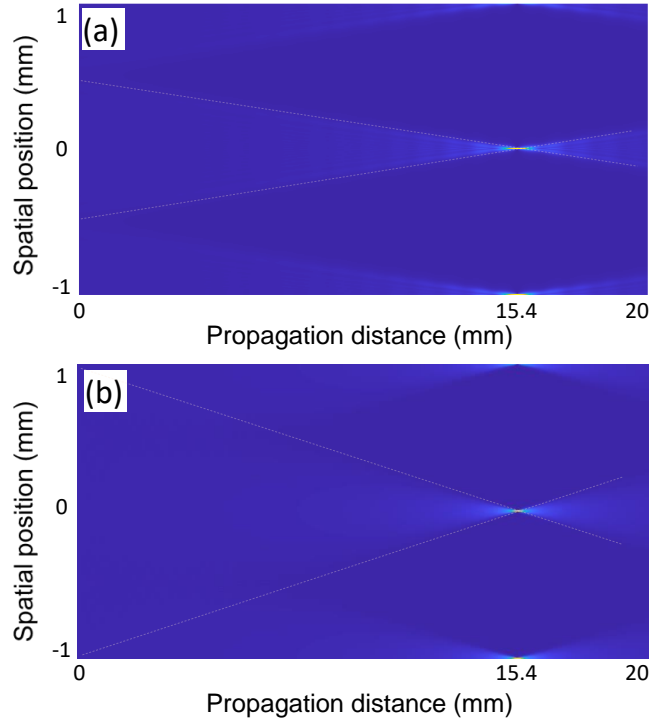


Fig. 8. Simulated propagating waves using the angular spectrum method. (a) High-frequency components of diffractions are eliminated and the point image is formed from the primary zone. (b) The diffraction behavior of the two-fold upsampled hologram is illustrated.

frequency of $1.25 \times 10^5 \text{m}^{-1}$, effectively functioning as a low-pass filter. The point image is formed from the primary zone which occupies half the width of the hologram aperture. The spatial resolution of the point image is $8 \mu\text{m}$, according to Eqs. (1) and (27). The spreading angle of the propagating wave is estimated to be 3.9° .

The diffraction behavior of a two-fold upsampled hologram was investigated. The upsampling process increases the pixel resolution from 256×256 pixels at $8 \mu\text{m}$ to 512×512 pixels at $4 \mu\text{m}$ by duplicating the pixel values. While the two-fold upsampled hologram retains the replica patterns, the calculation process is performed in the two-fold enhanced Fourier space, based on Eq. (27). There is no confinement by the upper bound frequency. The propagating behavior in Fig. 8(b) demonstrates that the central point image is formed through the entire region of the digital hologram. The diffracted wave converges at an angle of 7.2° before focusing on the point image, achieving a spatial resolution of $4 \mu\text{m}$.

This behavior clearly shows that the spatial frequency continuously increases across the shifted replica functions. Therefore, even the maximum spatial frequency in the undersampled hologram is defined by the entire aperture of the hologram in Eq. (1). Numerical simulation well matches with the theoretical description. The spatial resolution and viewing angle of the restored image are not fixed from the diffraction angle by a hologram pixel. It is apparent that these values vary depending on the focal distance in a digital hologram with finite space-bandwidth, in Fig. 9. Previously, it was reported that the viewing angle changes according to this relationship, as demonstrated in optical experiments [13].

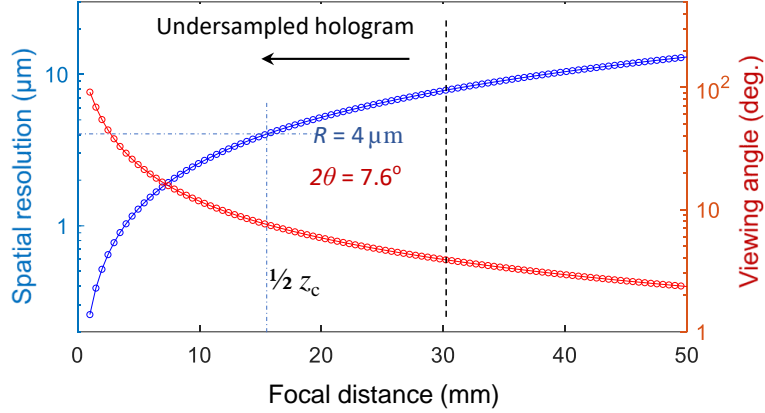


Fig. 9. Spatial resolution and viewing angle of the restored image as a function of focal distance. Both values are calculated from the point-source hologram synthesized at corresponding focal distances. The inset line indicates the values for the focused image at a distance of a half of z_c .

5. Angular spectrum expansion and discussions

Angular spectrum of a point-source hologram is represented by the transfer function, $G(f_x, f_y) = e^{ikz} \exp[-i\pi\lambda z(f_x^2 + f_y^2)]$. The transfer function in the Fourier space is a quadratic phase exponential, allowing the same sampling rule used for the response function in the real space to be applied here. Similarly, the sampled transfer function appears as the summation of shifted replica functions [15]:

$$\sum_m G(m\Delta f_x)\delta(f_x - m\Delta f_x) = \frac{1}{\Delta f_x} \sum_m c_m G\left(f_x + \frac{m}{\lambda z \Delta f_x}\right). \quad (28)$$

In the angular spectrum method, based on Eq. (26), the sampling condition can be determined by analyzing the embedded transfer function:

$$\frac{1}{\Delta f_x} \geq 2\lambda z |f_{x,\max}|. \quad (29)$$

The well-sampling condition with respect to the reconstruction distance z is derived as follows:

$$z \leq \frac{1}{2\lambda \Delta f_x |f_{x,\max}|} = \frac{N \Delta x^2}{\lambda}. \quad (30)$$

This condition is satisfied for distances below the critical distance z_c , other than the synthesized hologram using the Fresnel diffraction method with a single Fourier transform. Beyond this critical distance, aliased error occurs.

Figure 10 illustrates the diffraction behaviour for a hologram created at double the critical distance z_c , i.e., 61.6 mm. At this distance, the angular spectrum expands twofold, resulting in the formation of four replica patterns, according to Eq. (28). The hologram also shows aliasing, as depicted in Figs. 10(a) and 10(b). The expansion of the angular spectrum extends the hologram aperture, allowing the diffracted wave to propagate from twice the hologram aperture. This property maintains constant spatial resolution and spreading angle, regardless of distance.

In a previous study [14], it was shown that the undersampled angular spectrum corresponds to the undersampled hologram in the Wigner domain. The replicas in the undersampled angular

spectrum not only represent repetition but also extend higher spatial frequency components. From this, the increment of hologram aperture could be achievable via angular spectrum expansion.

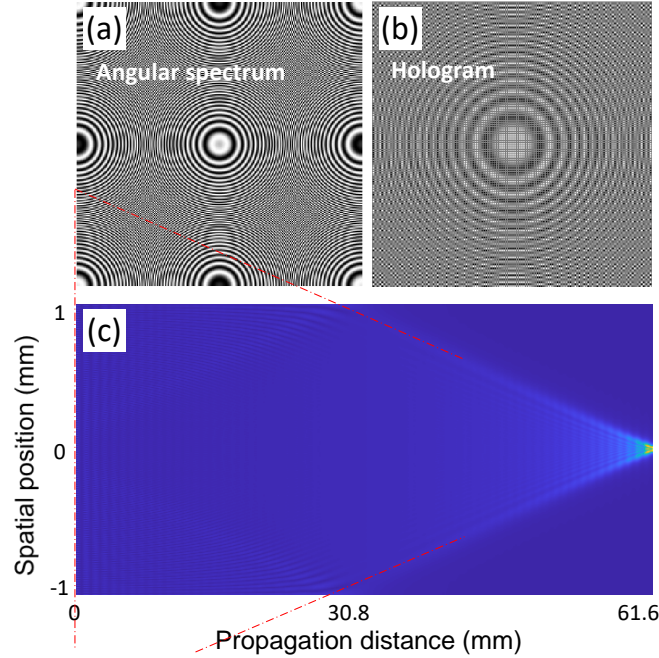


Fig. 10. Imaging behaviour of the point-source hologram made using the angular spectrum method. (a) Angular spectrum and (b) digital hologram synthesized at twice the critical distance z_c . (c) Diffractive waves propagating from the digital hologram.

The imaging performance depends on the space-bandwidth product of the digital hologram. A digitized device with a large space-bandwidth product is essential for acquiring high-resolution images at a large scale. Since the hologram undersampled by a low-resolution pixel includes components of higher spatial frequencies, a high-resolution and large-scale image can be obtained using a digitized device with finite bandwidth, provided that methods are developed to eliminate additive noise, such as high-order diffractions.

In holographic displays, the limited viewing angle remains a significant bottleneck for commercializing three-dimensional displays [19–22]. A 3D image is reconstructed by illuminating the pixelated modulator loading the digital hologram with a coherent plane wave. Commercial modulators can typically achieve only a few degrees of viewing angle at best. However, by leveraging the angular spectrum distribution properties of undersampled holograms, even commercial modulators can achieve a sufficiently large viewing angle. Previously, we explored a method to extend the viewing angle beyond the diffraction limit in a commercial spatial light modulator [13, 14]. This study further clarifies the proposed process, which primarily consists of two steps: First, an optimization algorithm is developed to synthesize the undersampled hologram using the object field beyond the diffraction scope by a hologram pixel. Second, a method to suppress high-order diffractions is employed. An upsampling process is utilized to eliminate high-order diffraction components, which can be achieved by attaching a high-definition grid to the pixelated modulator. Alternatively, if the diffractive waves exhibit distinct optical properties, such as polarization states, they can be entirely removed using a spatial filter.

The expansion of the spatial-frequency distribution into the undersampled regions can also be applied to the Rayleigh-Sommerfeld region. The optical kernel function used in this regime takes

the form, $\exp\left(i2\pi z\sqrt{\frac{1}{\lambda^2} - f_x^2 - f_y^2}\right)$, where the replica patterns may appear distorted. Moreover, it remains uncertain whether this approach is applicable to the evanescent field region. If these two issues can be theoretically resolved, this strategy could pave the way for meaningful advancements in super-resolution imaging.

6. Conclusions

A mathematical description of the angular spectrum distribution demonstrates that an under-sampled hologram at a lower sampling rate can reconstruct an image with the same spatial resolution and angular field of view as a properly sampled hologram. The spatial frequencies are found to be continuously distributed across the aliased replica functions. Moreover, the undersampled replica functions differ from the meaningless noise typically associated with conventional aliasing. Instead, they generate high-order diffractive waves that form replica images in the image plane. When these replica waves are effectively removed through suitable external operations, high-performance imaging can be achieved, surpassing the inherent space-bandwidth limitations of a digital hologram. One practical example of this concept addresses the issue of limited viewing angles in holographic displays. This technology provides an alternative approach to overcome the finite space-bandwidth constraints of digital holograms, paving the way for enhanced imaging performance.

Funding. This work was supported by Institute for Information & Communications Technology Promotion (IITP) grant funded by the Korea government (MSIP) (2021-0-00745)

Disclosures. The authors declare no conflicts of interest.

References

1. J. W. Goodman, Introduction to Fourier Optics (McGraw-Hill, 1996).
2. A. W. Lohmann, R. G. Dorsch, D. Mendlovic, Z. Zalevsky, and C. Ferreira, "Space-bandwidth product of optical signals and systems," *J. Opt. Soc. Am. A* **13**, 470-473 (1996).
3. P. Picart and J. Leval, "General theoretical formulation of image formation in digital Fresnel holography," *J. Opt. Soc. Am. A* **25**(7), 1744-1761 (2008).
4. D. P. Kelly, B. M. Hennelly, N. Pandey, T. J. Naughton, and W. T. Rhodes, "Resolution limits in practical digital holographic systems," *Opt. Eng.* **48**(9), 95801 (2009).
5. T. Lатыchevskaia and H.-W. Fink, "Inverted Gabor holography principle for tailoring arbitrary shaped three-dimensional beams," *Sci. Rep.* **6**, 26312 (2016).
6. B. G. Chae, "Analysis on angular field of view of holographic image dependent on hologram numerical aperture in holographic display," *Opt. Eng.* **59**(3), 035103 (2020).
7. F. Gori, "Fresnel transform and sampling theorem," *Opt. Commun.* **39**(5), 293-297 (1981).
8. L. Onural, "Sampling of the diffraction field," *Appl. Opt.* **39**(32), 5929-5935 (2000).
9. A. Stern and B. Javidi, "Analysis of practical sampling and reconstruction from Fresnel fields," *Opt. Eng.* **43**(1), 239-250 (2004).
10. B. G. Chae, "Analysis on image recovery for on-axis digital Fresnel hologram with aliased fringe generated from self-similarity of point spread function," *Opt. Commun.* **466**, 125609 (2020).
11. A. V. Oppenheim, A. S. Willsky, and S. H. Nawab, Signals and Systems (Prentice-Hall, 2010).
12. L. Onural, "Some mathematical properties of the uniformly sampled quadratic phase function and associated issues in Fresnel diffraction simulations," *Opt. Eng.* **43**(11), 2557-2563 (2004).
13. B. G. Chae, "Wide viewing-angle holographic display based on enhanced-NA Fresnel hologram," *Opt. Express* **29**(23), 38221-38236 (2021).
14. B. G. Chae, "Viewing-angle expansion in holographic displays implemented with a modulator having finite space-bandwidth," *Opt. Express* **31**(23), 37900-37910 (2023).
15. B. G. Chae, "Spatial resolution enhancement in holographic imaging via angular spectrum expansion," *Opt. Continuum* **3**(3), 263-277 (2024).
16. D. Mas, J. Garcia, C. Ferreira, L. M. Bernardo, and F. Marinho, "Fast algorithms for free-space diffraction patterns calculations," *Opt. Commun.* **164**, 233-245 (1999).
17. D. G. Voelz and M. C. Roggemann, "Digital simulation of scalar optical diffraction: revisiting chirp function sampling criteria and consequences," *Appl. Opt.* **48**(32), 6132-6142 (2009).
18. J.-P. Liu, "Controlling the aliasing by zero-padding in the digital calculation of the scalar diffraction," *J. Opt. Soc. Am. A* **29**(9), 1956-1964 (2012).

19. T. Kozacki, M. Kujawińska, G. Finke, B. Hennelly, and N. Pandey, "Extended viewing angle holographic display system with tilted SLMs in a circular configuration," *Appl. Opt.* **51**(11), 1771-1780 (2012).
20. K. Yamamoto, Y. Ichihashi, T. Senoh, R. Oi, and T. Kurita, "3D objects enlargement technique using an optical system and multiple SLMs for electronic holography," *Opt. Express* **20**(19), 21137-21144 (2012).
21. Y. Takaki and S. Uchida, "Table screen 360-degree three-dimensional display using a small array of high-speed projectors," *Opt. Express* **20**(8), 8848-8861 (2012).
22. M. Gopakumar, J. Kim, S. Choi, Y. Peng, and G. Wetzstein, "Unfiltered holography: optimizing high diffraction orders without optical filtering for compact holographic displays," *Opt. Lett.* **46**(23), 5822-5825 (2021).